nature physics

LETTERS

https://doi.org/10.1038/s41567-017-0041-4

Experimental discovery of nodal chains

Qinghui Yan[1,2], Rongjuan Liu[1], Zhongbo Yan[3], Boyuan Liu[1], Hongsheng Chen[2], Zhong Wang[3,4] and Ling Lu[1]*

Three-dimensional Weyl and Dirac nodal points[1] have attracted widespread interest across multiple disciplines and in many platforms but allow for few structural variations. In contrast, nodal lines[2–4] can have numerous topological configurations in momentum space, forming nodal rings[5–9], nodal chains[10–15], nodal links[16–20] and nodal knots[21,22]. However, nodal lines are much less explored because of the lack of an ideal experimental realization[23–25]. For example, in condensed-matter systems, nodal lines are often fragile to spin–orbit coupling, located away from the Fermi level, coexist with energy-degenerate trivial bands or have a degeneracy line that disperses strongly in energy. Here, overcoming all these difficulties, we theoretically predict and experimentally observe nodal chains in a metallic-mesh photonic crystal having frequency-isolated linear band-touching rings chained across the entire Brillouin zone. These nodal chains are protected by mirror symmetry and have a frequency variation of less than 1%. We use angle-resolved transmission measurements to probe the projected bulk dispersion and perform Fourier-transformed field scans to map out the dispersion of the drumhead surface state. Our results establish an ideal nodal-line material for further study of topological line degeneracies with non-trivial connectivity and consequent wave dynamics that are richer than those in Weyl and Dirac materials.

A nodal line is the extrusion of a Dirac cone, arguably the most intriguing two-dimensional band structure, into three-dimensional momentum space. They share the same local Hamiltonian $H(\mathbf{k}) = k_x\sigma_x + k_y\sigma_z$ that can be protected by the $\mathcal{PT}$ symmetry forbidding the mass term of σ_y in the whole Brillouin zone, where $\mathcal{P}$ is parity inversion and $\mathcal{T}$ is time-reversal symmetry. A single nodal line forms a closed ring, due to the periodicity of the Brillouin zone, and the Berry phase around the node is π. Surprisingly, it was recently proposed[11] that nodal rings can be chained together as shown in Fig. 1a. The Berry phase around the chain point, enclosing two nodal lines, is 0 ($=\pi+\pi$). We show, in Fig. 1b, that the local chain Hamiltonian can be written as $H(\mathbf{k}) = k_x\sigma_x + \left(k_yk_z + m_z\right)\sigma_z$, when the mass term $m_z = 0$. The vanishing mass $m_z = 0$ can be guaranteed by an extra symmetry other than $\mathcal{PT}$. One example is the mirror (or glide) symmetry $M_z = \sigma_x$ that flips z coordinates, shown in Fig. 1b as a yellow plane. In the presence of the mirror, the two nodal lines cross at the origin. The red nodal line locates at the intersection between the planes of $k_x = 0$ and $k_y = 0$ and the blue nodal line locates at the intersection between the planes of $k_x = 0$ and $k_z = 0$. When the mirror symmetry is broken ($m_z \neq 0$), the chain point is lifted and the nodal lines become hyperbolic.

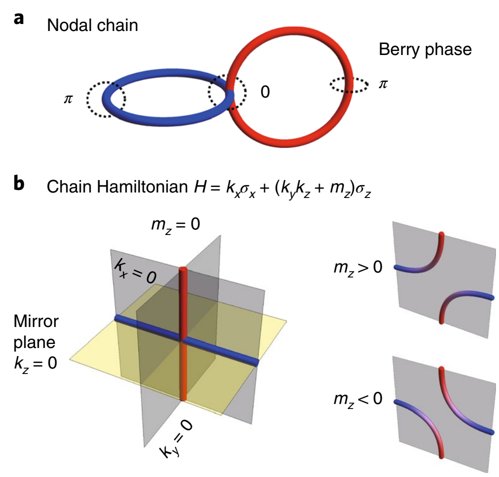

Fig. 1 | Nodal-chain Hamiltonian and stability. a, Illustration of the simplest chain structure between two rings. The Berry phase around the chain point is 0, in contrast to the π Berry phase of nodal lines. **b**, The chain point is the crossing between two nodal lines defined between three zero planes. The third plane in yellow represents the mirror plane protecting the chain point. When the mirror symmetry is broken by the mass term m_z, the chain point splits.

We designed a metallic-mesh three-dimensional photonic crystal with frequency-isolated nodal chains. The structure is shown in Fig. 2a. The yellow box denotes the cubic unit cell of space group $Pm\bar{3}m$, no. 221. Intersecting at the centre of the unit cell are three square rods along x, y and z directions, respectively. Numerically, we treat the metallic surfaces as perfect electric conductors, which is a good approximation for metals at microwave frequencies. We note that similar metallic-mesh structure has also been used for low-frequency plasmons[26], particle accelerators[27], novel metamaterials[28] and invisible medium[29].

Shown in Fig. 2b, the third and the fourth bands cross linearly, forming line degeneracies of nodal chains. The chain structure is plotted in Fig. 2c, where all nodal lines are chained across the entire the Brillouin zone. There are three red rings centred at the X points on each face and three blue rings centred at the M points on each hinge. The same colored rings are related by the C_3 rotation symmetry along ⟨111⟩ directions. Each blue ring is chained with the neighbouring red rings perpendicular to it. All chain points lie in and are protected by the {001} mirror planes. The band-structure evolution of metallic meshes of various filling ratios are presented in the Supplementary Information.

[1]Institute of Physics, Chinese Academy of Sciences/Beijing National Laboratory for Condensed Matter Physics, Beijing, China. [2]College of Information Science and Electronic Engineering, State Key Laboratory of Modern Optical Instrumentation, Zhejiang University, Hangzhou, China. [3]Institute for Advanced Study, Tsinghua University, Beijing, China. [4]Collaborative Innovation Center of Quantum Matter, Beijing, China. Qinghui Yan and Rongjuan Liu contributed equally to this work. *e-mail: linglu@iphy.ac.cn

© 2018 Macmillan Publishers Limited, part of Springer Nature. All rights reserved.

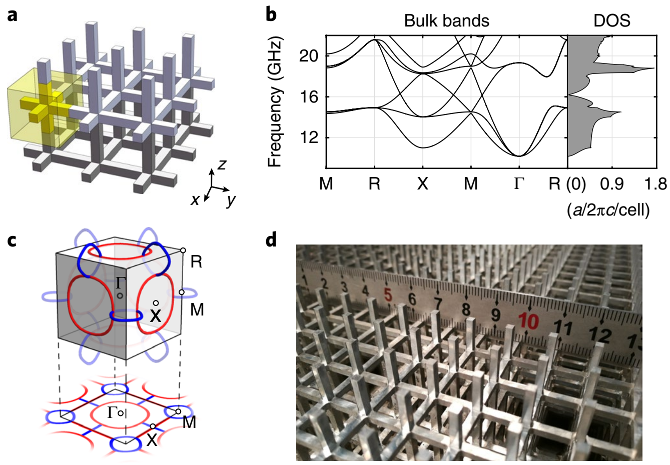

Fig. 2 | Nodal-chain photonic crystal. a, An illustration of the metallic-mesh three-dimensional photonic crystal. The yellow cube denotes a symmetric simple-cubic unit cell. **b**, The bulk band structure and DOS. The nodal-chain frequency is about 16.2 GHz. **c**, The structure of nodal chains in the Brillouin zone. The three blue rings are chained with the three red rings. **d**, The top surface of the sample made of aluminium alloy. The bottom surface is a flat mesh. The lattice constant is 11.6 mm and the rod width is 2 mm.

An important feature of this nodal chain is the low dispersion of the degeneracy frequencies, which is below 1% for the variation ($\Delta\omega/\omega_{\mathrm{middle}}$) in the entire Brillouin zone. This is supported by the density of states (DOS) calculations[30] on the right of Fig. 2b. There is a clear dip in the DOS increasing linearly away from the nodal-chain frequency.

In experiment, we adopted aluminium as the material of choice for its high conductivity, low weight and low cost. The fabricated sample is shown in Fig. 2a with a lattice constant of 11.6 mm and a rod width of 2 mm. The resulting nodal-chain frequencies are very close to 16.2 GHz, as shown in Fig. 2b. The sample is stacked with nine identical layers and each layer has 30 × 30 unit cells. Every layer was milled and drilled from a plain aluminum plate. For assembling, handling and alignment, we reserved frames around each layer. The final size for one layer is 37 cm × 37 cm × 10.44 cm.

We carried out angle-resolved transmission to measure the nodal-chain bulk states. As shown in Fig. 3a, we used a similar set-up as in ref. [5] to detect the frequency-resolved transmission as a function of the incident angle. As a result, angle-resolved transmission measures the bulk states projected along the normal direction (z) of the incident surface of the sample. In the in-plane directions on the surface, momenta are conserved. Figure 3b shows the [001] projection of nodal chains from numerical calculations, illustrated in Fig. 2c. A vector network analyser was used to collect data. A pair of prisms, with refractive index of 4, were used to increase the incident momenta and probe more areas in the reciprocal space (not shown in Fig. 3a). For comparison, we present the results without the prisms in Supplementary Information.

The comparisons between experimental results and projected band structures are shown in Fig. 3c–f for four different angles of $\theta = 0$, 15, 30 and 45°. With over 25 dB attenuation in bandgaps, results are clear and in good agreement with theory. The transmission data for separate polarization channels are presented in the Supplementary Information.

We performed Fourier-transformed field scans to measure the surface states of our nodal-chain sample. A nodal-line material is known to support a drumhead surface state, which is a sheet of surface dispersion enclosed by the projected nodal-line bulk states in the surface Brillouin zone. We form a surface by placing an aluminum plate 1 mm above the sample (001) surface, in order to isolate the free-space photon modes while leaving space for the near-field scanning probes. The set-up is shown in Fig. 4a and the surface band structure is plotted in Fig. 4b. The surface state is highlighted in red.

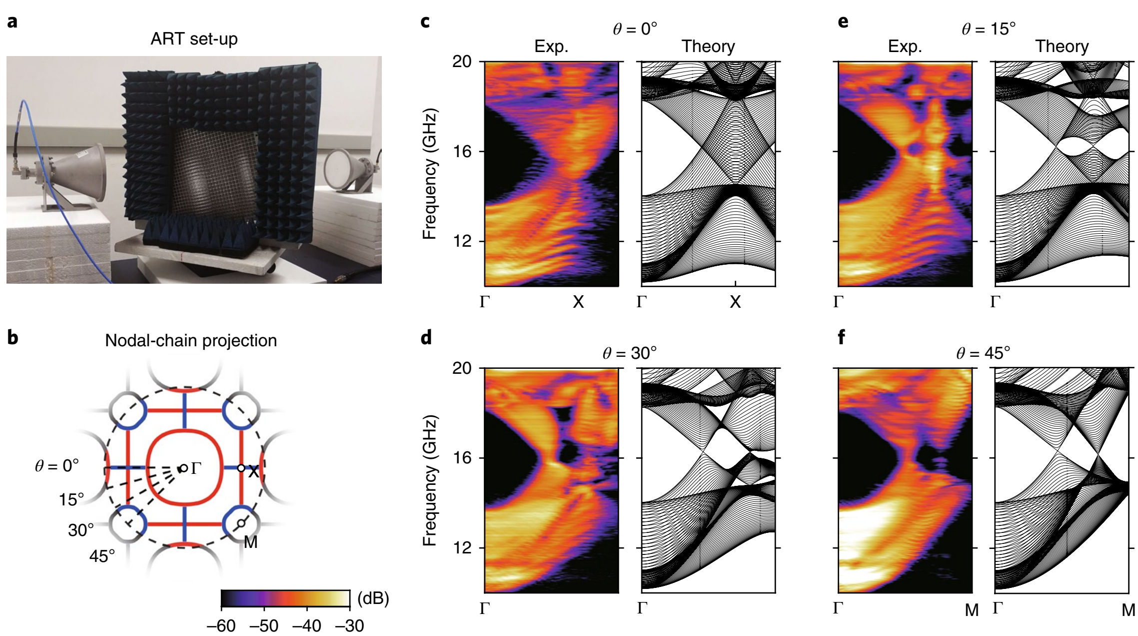

Fig. 3 | Angle-resolved transmission (ART) measurement of nodal-chain bulk states. a, The experimental set-up. **b**, Projective view of nodal chain in [001] direction. The dashed circle is the light cone in the prism at 16.2 GHz, which is the maximum momentum of the incident photon on the sample after the prism. Four dashed radii denote the four scan directions. **c–f**, Bulk experimental data compared with theoretical calculations for different θ values. The agreement is excellent.

© 2018 Macmillan Publishers Limited, part of Springer Nature. All rights reserved.

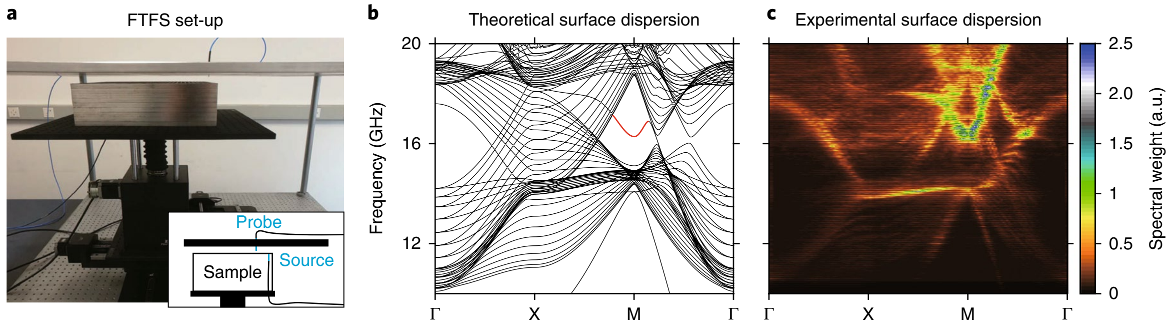

Fig. 4 | Fourier-transformed field (FTFS) scan measurement of the drumhead surface state. We measured the bottom surface of a flat mesh. **a**, Photograph and schematic illustration of the two-dimensional profiler. **b**, Theoretical calculation of the surface band structure. The supercell consists of 11 unit cells, with a 1 mm air gap to the upper perfect electrical conductor boundary. Plotted in red is the drumhead surface dispersion. **c**, The experimental Fourier-transformed field scans plotted in a linear scale. The surface modes appear at about 17 GHz, which matches the theoretical prediction. Other surface dispersions and some bulk bands can also be seen with lower intensities.

During the field scan, a broadband source was fixed inside the sample to excite both the surface and the bulk states. The probe was placed inside the hole in the centre of the aluminum board. The details of the profiler are presented in the Supplementary Information. During the measurement, the sample moved in plane on the guiding rails and the probe scanned across the sample surface point by point. Both the amplitude and the phase of the local fields were recorded at each frequency by the network analyser.

We then Fourier-transformed the field data from real space to reciprocal space and summed up the amplitudes in all equivalent Bloch momenta to the first Brillouin zone. Details of data processing are in the Supplementary Information. In Fig. 4c, the resulting intensity map is directly compared with the dispersion calculations. The drumhead surface modes at about 17 GHz are consistently seen in both theory and experimental data. A doubly degenerate drumhead due to the C_{4v} symmetry, of a different surface termination, is plotted in the Supplementary Information.

Our finding may inspire searches for ideal nodal lines in other material platforms, and stimulate experimental realizations of nontrivial nodal-line structures, such as nodal links[17] and nodal knots[22].

Data availability. The data that support the plots within this paper and other findings of this study are available from the corresponding author upon reasonable request.

Received: 21 June 2017; Accepted: 18 December 2017;
Published online: 19 February 2018

References

1. Armitage, N. P., Mele, E. J. & Vishwanath, A. Weyl and Dirac semimetals in three dimensional solids. Preprint at https://arxiv.org/abs/1705.01111 (2017).
2. Burkov, A. A., Hook, M. D. & Balents, L. Topological nodal semimetals. *Phys. Rev. B* **84**, 235126 (2011).
3. Lu, L., Fu, L., Joannopoulos, J. D. & Soljacic, M. Weyl points and line nodes in gyroid photonic crystals. *Nat. Photon.* **7**, 294–299 (2013).
4. Fang, C., Weng, H., Dai, X. & Fang, Z. Topological nodal line semimetals. *Chin. Phys. B* **25**, 117106 (2016).
5. Lu, L. et al. Experimental observation of Weyl points. *Science* **349**, 622–624 (2015).
6. Kim, Y., Wieder, B. J., Kane, C. L. & Rappe, A. M. Dirac line nodes in inversion-symmetric crystals. *Phys. Rev. Lett.* **115**, 036806 (2015).
7. Yu, R., Weng, H., Fang, Z., Dai, X. & Hu, X. Topological node-line semimetal and Dirac semimetal state in antiperovskite Cu_3PdN. *Phys. Rev. Lett.* **115**, 036807 (2015).
8. Fang, C., Chen, Y., Kee, H.-Y. & Fu, L. Topological nodal line semimetals with and without spin–orbital coupling. *Phys. Rev. B* **92**, 081201 (2015).
9. Kobayashi, S. et al. Crossing-line-node semimetals: general theory and application to rare-earth trihydrides. *Phys. Rev. B* **95**, 245208 (2017).
10. Weng, H. et al. Topological node-line semimetal in three-dimensional grapheme networks. *Phys. Rev. B* **92**, 045108 (2015).
11. Bzdusek, T., Wu, Q., Riiegg, A., Sigrist, M. & Soluyanov, A. A. Nodal-chain metals. *Nature* **538**, 75–78 (2016).
12. Kawakami, T. & Hu, X. Symmetry-guaranteed and accidental nodal-line semimetals in fcc lattice. Preprint at https://arxiv.org/abs/1611.07342 (2016).
13. Yu, R., Wu, Q., Fang, Z. & Weng, H. From nodal chain semimetal to Weyl semimetal in HfC. *Phys. Rev. Lett.* **119**, 036401 (2017).
14. Wang, S.-S., Liu, Y., Yu, Z.-M., Sheng, X.-L. & Yang, S. A. Hourglass Dirac chain metal in rhenium dioxide. Preprint at https://arxiv.org/abs/1705.01424 (2017).
15. Feng, X., Yue, C., Song, Z., Wu, Q. & Wen, B. Topological Dirac nodal-net fermions in AlB_2-type TiB_2 and ZrB_2. Preprint at https://arxiv.org/abs/1705.00511 (2017).
16. Chen, W., Lu, H.-Z. & Hou, J.-M. Topological semimetals with a double-helix nodal link. *Phys. Rev. B* **96**, 041102 (2017).
17. Yan, Z. et al. Nodal-link semimetals. *Phys. Rev. B* **96**, 041103 (2017).
18. Chang, P.-Y. & Yee, C.-H. Weyl-link semimetals. *Phys. Rev. B* **96**, 081114 (2017).
19. Zhong, C. et al. Three-dimensional pentagon carbon with a genesis of emergent fermions. *Nat. Commun.* **8**, 15641 (2017).
20. Chang, G. et al. Topological Hopf and chain link semimetal states and their application to Co_2MnGa. *Phys. Rev. Lett.* **119**, 156401 (2017).
21. Ezawa, M. Topological semimetals carrying arbitrary Hopf numbers: Fermi surface topologies of a Hopf link, Solomon's knot, trefoil knot, and other linked nodal varieties. *Phys. Rev. B* **96**, 041202 (2017).
22. Bi, R., Yan, Z., Lu, L. & Wang, Z. Nodal-knot semimetals. *Phys. Rev. B* **96**, 201305 (2017).
23. Bian, G. et al. Topological nodal-line fermions in spin–orbit metal $PbTaSe_2$. *Nat. Commun.* **7**, 10556 (2016).
24. Schoop, L. M. et al. Dirac cone protected by non-symmorphic symmetry and three-dimensional Dirac line node in Zr-SiS. *Nat. Commun.* **7**, 11696 (2016).
25. Chen, C. et al. Dirac line nodes and effect of spin–orbit coupling in the nonsymmorphic critical semimetals MSiS (M = Hf, Zr). *Phys. Rev. B* **95**, 125126 (2017).
26. Pendry, J. B., Holden, A. J., Stewart, W. J. & Youngs, I. Extremely low frequency plasmons in metallic mesostructures. *Phys. Rev. Lett.* **76**, 4773 (1996).
27. Shapiro, M. A., Sirigiri, J. R., Temkin, R. J. & Shvets, G. 3D metallic lattices for accelerator applications. In *Proceedings of the Particle Accelerator Conference, 2005. PAC 2005* 1838–1840 (IEEE, 2005).
28. Chen, W.-J. & Chan, C. T. Metamaterials with index ellipsoids at arbitrary k-points. Preprint at https://arxiv.org/abs/1611.08099 (2016).
29. Ye, D., Lu, L., Joannopoulos, J. D., Soljacic, M. & Ran, L. Invisible metallic mesh. *Proc. Natl Acad. Sci.USA* **113**, 2568–2572 (2016).
30. Liu, B., Johnson, S. G., Joannopoulos, J. D. & Lu, L. Generalized Gilat–Raubenheimer method for density-of-states calculation in photonic crystals. Preprint at https://arxiv.org/abs/1711.07993 (2017).

© 2018 Macmillan Publishers Limited, part of Springer Nature. All rights reserved.

Acknowledgements
We thank Yang He, Chen Fang and Hongming Weng for discussions. The authors were supported by the National Key R&D Program of China under Grant Nos 2017YFA0303800 and 2016YFA0302400 and by NSFC under Project Nos 11721404 (L.L.), 11674189 (Z.Y., Z.W.), 61625502 (H.C.), 61574127 (H.C.), the Top-Notch Young Talents Program (H.C.) and the National Thousand Young Talents Program (L.L.) of China.

Author contributions
L.L. proposed and led the project. R.L. fabricated the sample. Q.Y. and R.L. made the measurements. Q.Y. processed the data and carried out the calculations. Z.W. and Z.Y. came up with the *k.p* model and enhanced the theoretical understanding. All authors contributed to the discussion and writing of the manuscript.

Competing interests
The authors declare no competing financial interests.

Additional information
Supplementary information is available for this paper at https://doi.org/10.1038/s41567-017-0041-4.

Reprints and permissions information is available at www.nature.com/reprints.

Correspondence and requests for materials should be addressed to L.L.

Publisher's note: Springer Nature remains neutral with regard to jurisdictional claims in published maps and institutional affiliations.

© 2018 Macmillan Publishers Limited, part of Springer Nature. All rights reserved.

nature physics

SUPPLEMENTARY INFORMATION

https://doi.org/10.1038/s41567-017-0041-4

In the format provided by the authors and unedited.

Experimental discovery of nodal chains

Qinghui Yan[1,2], Rongjuan Liu[1], Zhongbo Yan[3], Boyuan Liu[1], Hongsheng Chen[2], Zhong Wang[3,4] and Ling Lu[1*]

[1]Institute of Physics, Chinese Academy of Sciences/Beijing National Laboratory for Condensed Matter Physics, Beijing, China. [2]College of Information Science and Electronic Engineering, State Key Laboratory of Modern Optical Instrumentation, Zhejiang University, Hangzhou, China. [3]Institute for Advanced Study, Tsinghua University, Beijing, China. [4]Collaborative Innovation Center of Quantum Matter, Beijing, China. Qinghui Yan and Rongjuan Liu contributed equally to this work. *e-mail: linglu@iphy.ac.cn

© 2018 Macmillan Publishers Limited, part of Springer Nature. All rights reserved.

Supplementary Information for "Experimental discovery of nodal chains"

Qinghui Yan†,[1,2] Rongjuan Liu†,[1] Zhongbo Yan,[3] Boyuan Liu,[1] Hongsheng Chen,[2] Zhong Wang,[3,4] and Ling Lu[1,*]

[1] *Institute of Physics, Chinese Academy of Sciences/Beijing National Laboratory for Condensed Matter Physics, Beijing 100190, China*

[2] *State Key Laboratory of Modern Optical Instrumentation, College of Information Science and Electronic Engineering, Zhejiang University, Hangzhou 310027, China*

[3] *Institute for Advanced Study, Tsinghua University, Beijing 100084, China*

[4] *Collaborative Innovation Center of Quantum Matter, Beijing 100871, China*

[*] linglu@iphy.ac.cn

†The first two authors contributed equally to this work.

CONTENTS

I. EVOLUTION AND ANNIHILATION OF NODAL CHAINS

Nodal rings in Fig. 2 of the main text can be annihilated by varying the thickness of the metallic mesh. As shown in Fig. S1, by increasing the width of the square rod, blue nodal rings gradually shrink into points at the *M* points. Then, the red nodal rings shrink into a six-fold degenerated point at *R* point and opened a band gap between the third and fourth bands.

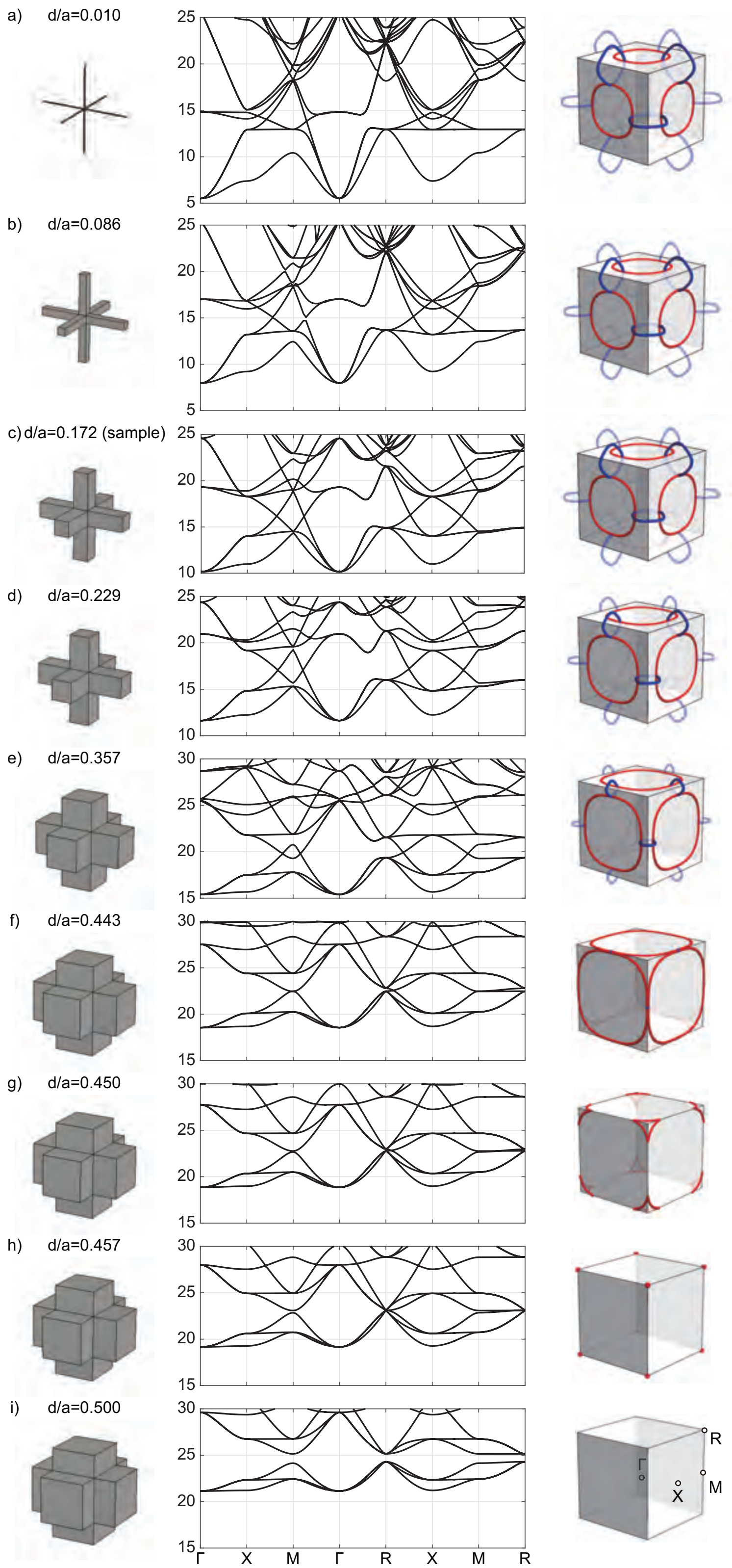

FIG. S1. Annihilation of nodal chains. (a), ..., (e) By increasing the size of the square rod, blue nodal rings gradually shrink into (f) nodal points at the *M* points, and break up into (g) individual nodal rings. (h) The rings shrink into a six-fold degenerate point at the *R* points. (i) Finally, a band gap is opened.

II. DETAILED PARAMETERS OF THE 2D PROFILER

During the field scan, the size of the surface air-gap variation is controlled within 1±0.2mm throughout the measurement. This not only requires the flatness of the PEC boundary, but also the parallelism of the three surfaces: the lower surface of the PEC board, the upper surface of the sample, and the surface that the guiding rails move along.

The size of the aluminum board, in our experiment, is 1.4m × 1.4m × 1.5cm. Its length and width should be at least twice of the size of the sample surface, in order to cover its upper surface (37cm × 37cm) throughout the scan. The thickness of the board should be larger than 1cm to reduce the bending caused by gravity.

The spatial resolution of the scanned data is limited by the physical size of the probe. In our 2D profiler, the probe is placed inside a Φ2mm hole centered at the PEC board without touching to it. Two types of probes are available: JSMA-KFD1537 (Φ0.43mm × 5mm) and JSMA-KFD1538 (Φ0.87mm × 10mm), both designed and fabricated by Huada International Electronics & Technology Co., Ltd.

For measurements inside a small air-gap of 1mm (Fig. 4 in the maintext), we used JSMA-KFD1537 that is short enough not to scraping the sample surface. We used JSMA-KFD1538 to measure the surface state of an 8mm air gap and the result is shown in Fig. S2.

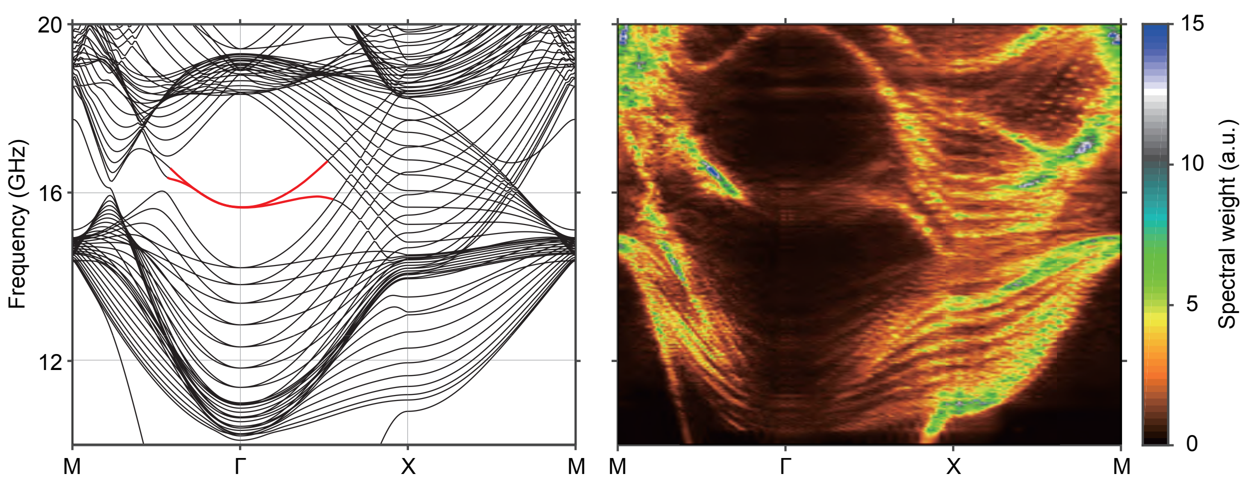

FIG. S2. FTFS measurement of the drumhead surface state. Different from Fig. 4 in the main text, the data is measured by JSMA-KFD1538 with an 8mm air gap. The theoretical calculation on the left is in good agreement with the experimental results.

III. DATA PROCESSING IN FTFS

We perform equi-spacing sampling in square grid to scan the surface wave. In our experiments, both directions are scanned 35cm with 101 sample points. Then we Fourier-transform the fields and sum up the information in every Brillouin zone. Below is an estimation on the resolution of a Brillouin zone.

The range of the reciprocal space is determined by the scanning intervals. In our experiment,

$$k_{range} = \frac{2\pi}{35cm/100} \tag{1}$$

The size of the Brillouin zone is

$$k_{BZrange} = \frac{2\pi}{1.16cm} \tag{2}$$

The reciprocal space covers

$$k_{range}/k_{BZrange} \approx 3.3 \tag{3}$$

The resolution of each Brillouin zone is

$$100/3.3 \approx 30 \tag{4}$$

, which equals the number of real-space unit cells in each direction.

IV. SURFACE DISPERSION MEASUREMENT BY FTFS

As an example, we show the procedures for getting the data in Fig. S2.

From the above section we know the maximum resolution of a Brillouin zone is determined only by the number of unit cells of the sample. This inspires us to increase the resolution by enlarging the scan range in real space. We take four measurements by putting the source at each corner of the sample surface for field excitation. Then we stitch them together as shown in Fig. S3a. With this trick, the resolution can be doubled. In principle, each field should be measured independently. Nevertheless, due to the C_{4v} symmetry of the $\{001\}$ surface, we measured one of the four cases, and flipped the axises for the rest three fields, as shown in Fig. S3a.

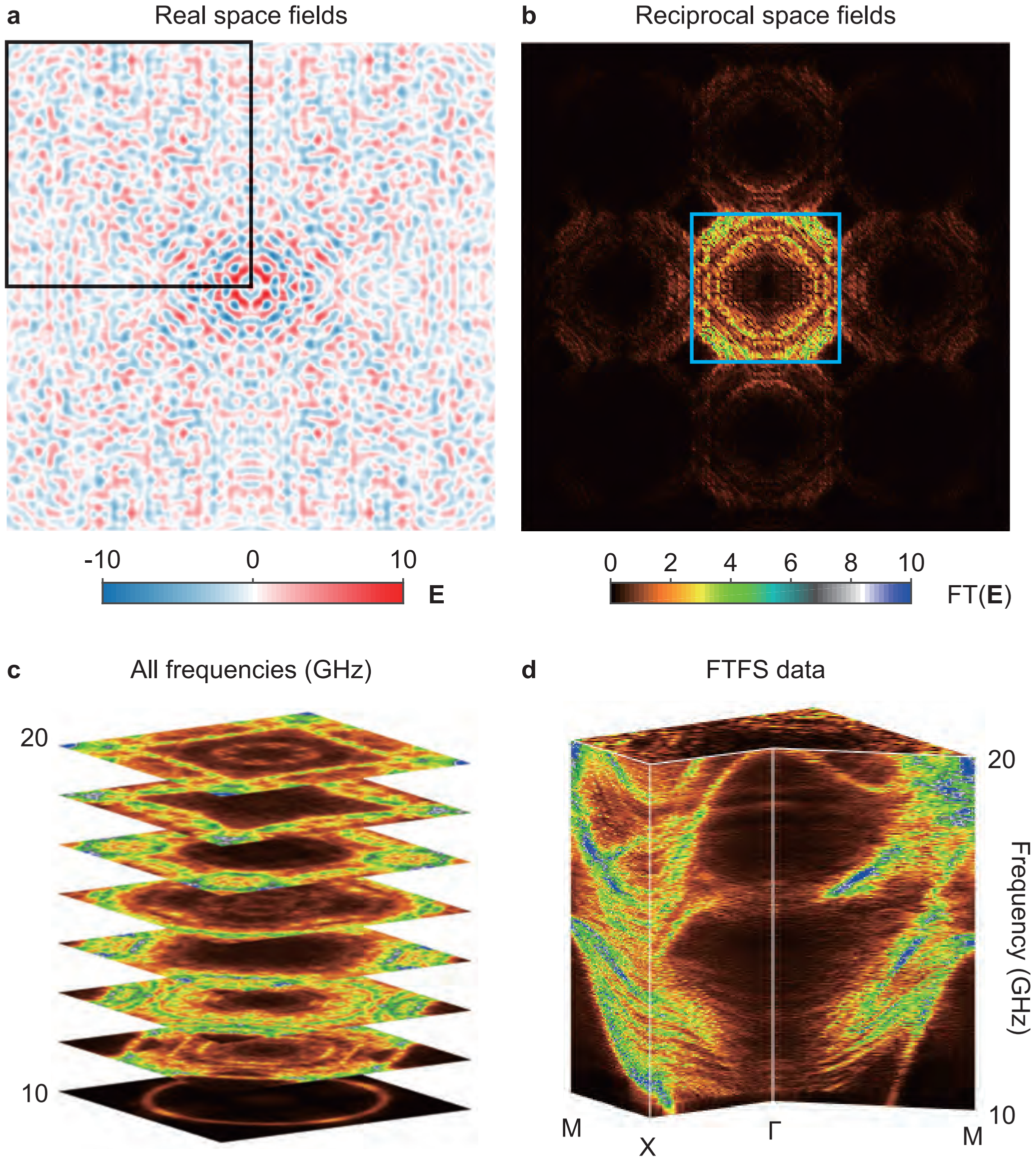

FIG. S3. Steps of FTFS data processing. (a)The electric fields in real space scanned at 13.12 GHz. Due to the C_{4v} surface symmetry, we put the source at the corner of the sample and measure the field. Then we flip the field to get the other three fields and stitch them together. (b) Reciprocal space intensity by Fourier transform. The cyan square denotes the first Brillouin zone. (c) Multiple slices of the Brillouin zone along frequency. Each figure is the summation of amplitudes from all equivalent Bloch momenta. (d) The 3D bulk view of Brillouin zone along frequency. By interpolation, we plot the FTFS data on high-symmetry planes in perspective view. The drumhead surface states can be seen in middle of the plot.

V. ART DATA WITHOUT PRISMS

In ART, the momentum scan range is proportional to the index of the prisms. Therefore, as long as the data quality is good enough, using prisms is always a better choice. Nevertheless, using prisms more or less induces extra scattering and alters the coupling efficiency of the incident wave. In Fig. S4, we show the measurement data without prisms as a comparison to those with prisms of the Fig. 3 in the main text.

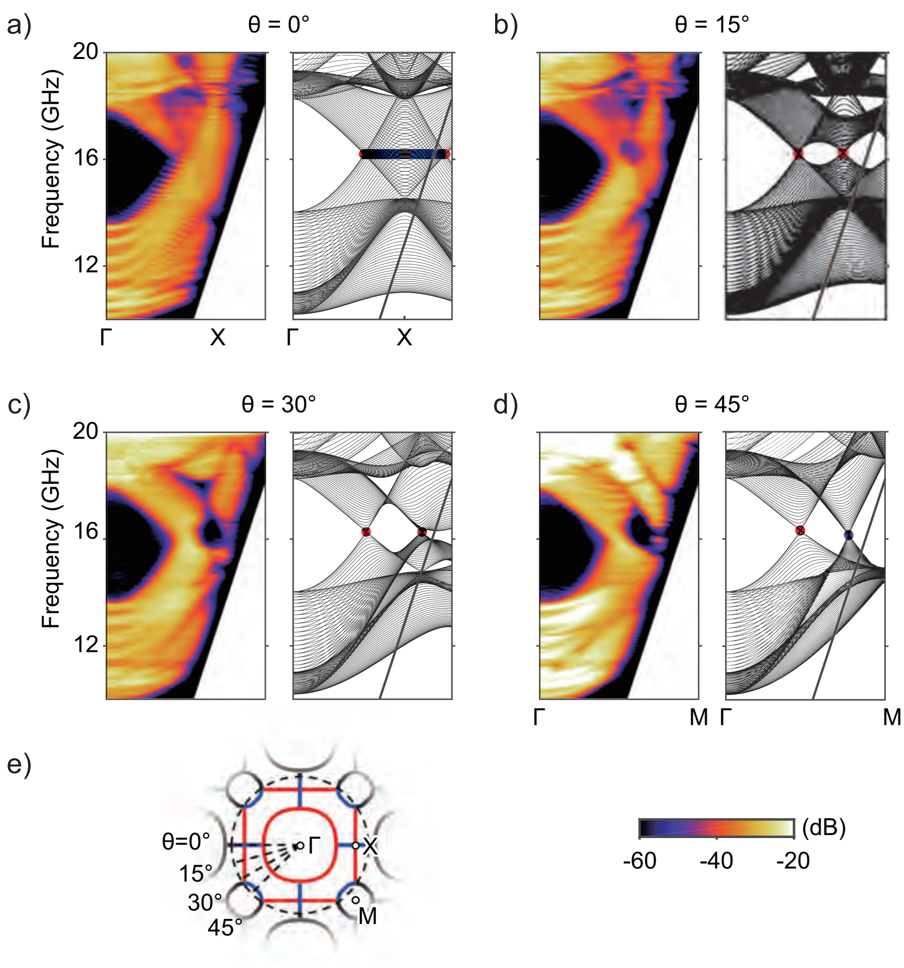

FIG. S4. The comparison between numerical calculations and ART experimental results without prisms. The range of measurement is limited within the light line. (a), (b), (c), (d) Bulk experimental data without prisms, compared with the corresponding theoretical calculations for different θ values. (e) Projective view of the nodal chain in [001] direction. The dashed circle is the light cone in air at 16.2 GHz, which is the maximum momentum of the incident photon. Four dashed radii denote the four scan directions.

VI. POLARIZATION-DEPENDENT ART DATA

Art data is polarization dependent. A single incident/recieving polarization excites only part of the bulk bands. Here, we consider s-polarization and p-polarization, whose electric fields and magnetic fields are vertically aligned, respectively. For each subplot in Fig. 3 in the main text, we measure four cases of transmittance: wave incident with an s-polarization antenna to an s-polarization receving antenna (T_s^s for short), T_p^p, T_p^s, and T_s^p. We switch polarization by rotating the linearly-polarized horn antenna by 90 degrees. Each case is calibrated by the transmission when two antennas directly touch. Before calibration, the intensities of T_s^s and T_p^p were higher than T_p^s and T_s^p; after that, they are of the same order of magnitude. At last, we sum up all the cases, which light up all parts of the photonic bands.

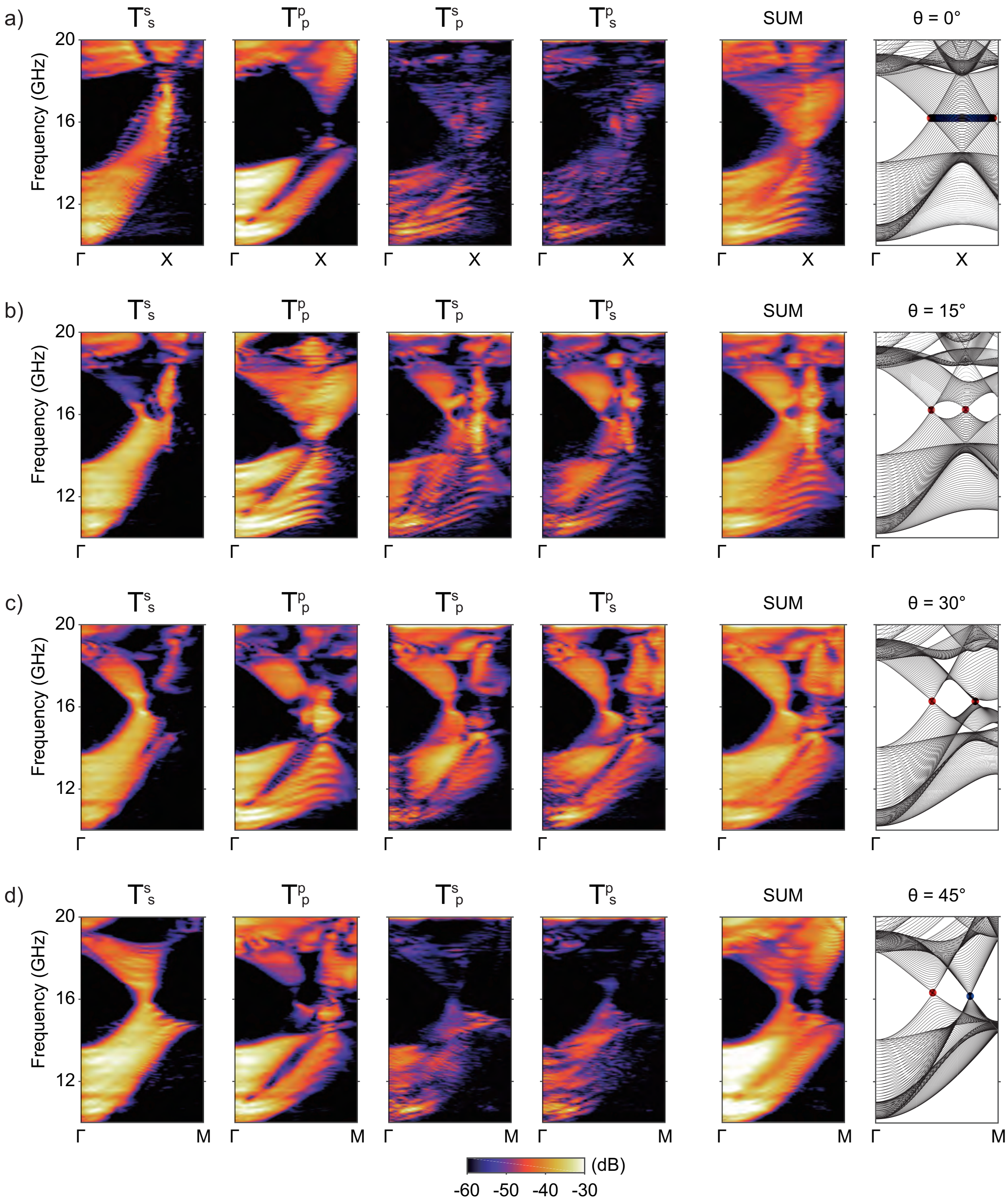

FIG. S5. For each subplot in Fig. 3 of main text, we display their polarization-dependent transmission: T_s^s, T_p^p, T_p^s, and T_s^p, formatted as $T_{receiving-polarization}^{incident-polarization}$. Each case excites different parts of bands. (a), (b), (c), (d) show the transmission data for different θ values, and compare the results with theoretical calculations.